Acoustic wave-equation-based earthquake location

Ping Tong,[1] Dinghui Yang,[2] Qinya Liu,[3] Xu Yang[4] and Jerry Harris[1]

[1]*Department of Geophysics, Stanford University, California, USA. E-mail: tongping85@gmail.com*
[2]*Department of Mathematical Sciences, Tsinghua University, Beijing, China*
[3]*Department of Physics, University of Toronto, Ontario, Canada*
[4]*Department of Mathematics, University of California, Santa Barbara, California, USA*

SUMMARY

We present a novel earthquake location method using acoustic wave-equation-based traveltime inversion. The linear relationship between the location perturbation $(\delta t_0, \delta \mathbf{x}_s)$ and the resulting traveltime residual δt of a particular seismic phase, represented by the traveltime sensitivity kernel $\mathbf{K}(t_0, \mathbf{x}_s)$ with respect to the earthquake location $(t_0, \mathbf{x}_s)$, is theoretically derived based on the adjoint method. Traveltime sensitivity kernel $\mathbf{K}(t_0, \mathbf{x}_s)$ is formulated as a convolution between the forward and adjoint wavefields, which are calculated by numerically solving two acoustic wave equations. The advantage of this newly derived traveltime kernel is that it not only takes into account the earthquake–receiver geometry but also accurately honours the complexity of the velocity model. The earthquake location is obtained by solving a regularized least-squares problem. In 3-D realistic applications, it is computationally expensive to conduct full wave simulations. Therefore, we propose a 2.5-D approach which assumes the forward and adjoint wave simulations within a 2-D vertical plane passing through the earthquake and receiver. Various synthetic examples show the accuracy of this acoustic wave-equation-based earthquake location method. The accuracy and efficiency of the 2.5-D approach for 3-D earthquake location are further verified by its application to the 2004 Big Bear earthquake in Southern California.

Key words: Numerical solutions; Inverse theory; Computational seismology; Theoretical seismology.

1 INTRODUCTION

The earthquake location can be defined as its origin time t_0 and hypocentre $\mathbf{x}_s$, the initiating point of fault rupture or explosion (Thurber 2014). Determining the location of an earthquake is a fundamental seismological problem and essential for many quantitative seismological analyses (e.g. Pesicek *et al.* 2014; Thurber 2014). For example, the key component of the earthquake early warning system is to detect the *P*-wave and immediately determine the location and size of the quake (http://www.usgs.gov). In earthquake seismology, the studies of earthquake dynamics and tectonic processes require good knowledge of earthquake locations (Waldhauser & Ellsworth 2000). Meanwhile, investigating the relationship between the generation of earthquakes and structural heterogeneities in seismogenic zone relies on precise locations of earthquakes (e.g. Huang & Zhao 2013; Lin 2013). In the fields of exploration seismology, such as geothermal exploration, hydraulic fracturing, reservoir monitoring, carbon sequestration and mining operations, accurately locating earthquakes is important for exploring the underground properties and guiding future activities (e.g. Castellanos & van der Baan 2013; Poliannikov *et al.* 2014). In addition, earthquake location techniques also have applications in locating and monitoring nuclear explosion tests (e.g. Wen & Long 2010; Zhang & Wen 2015).

As one of the oldest research problems in seismology, earthquake location can be determined by a wide variety of techniques nowadays. Some of the first quantitative methods for locating earthquakes, such as the methods of circles, hyperbolas, and coordinates, were devised in the late of the nineteenth century (Milne 1886; Thurber 2014). These methods still have some applications in early warning systems, tectonic and volcanic processes (e.g. Font *et al.* 2004; Horiuchi *et al.* 2005; Sumiejski *et al.* 2009) as mentioned by Thurber (2014). Geiger (1910, 1912) developed an iterative least-squares method for earthquake location, which has become the most widely used one so far (e.g. Thurber

1985; Ge 2003a,b; Thurber 2014). For Geiger's method, the relationship between the traveltime perturbation δt of a particular seismic phase (such as *P*- or *S*-wave) and the earthquake location perturbation $(\delta t_0, \delta \mathbf{x}_s)$ can be written as

$$\delta t = \delta t_0 + \frac{\partial t}{\partial \mathbf{x}_s} \cdot \delta \mathbf{x}_s = \delta t_0 - \frac{1}{V_{\mathbf{x}_s}} \frac{d\mathbf{x}_s}{dl} \cdot \delta \mathbf{x}_s, \tag{1}$$

where $V_{\mathbf{x}_s}$ is the velocity of the considered seismic phase at the source $\mathbf{x}_s$ and l is the length parameter along the ray path (e.g. Thurber 1985; Ge 2003b; Chen *et al.* 2006; Thurber 2014). The Simplex method (e.g. Prugger & Gendzwill 1988; Rabinowitz 1988) is another primary algorithm for earthquake location (Ge 2003a,b). It utilizes a curve-fitting technique to search the minimums (optimal source locations) of the objective function in terms of the traveltime residuals. Different from Geiger's method, the Simplex method does not require derivative calculations (Prugger & Gendzwill 1988). It is also computationally efficient and stable (Rabinowitz 1988; Ge 2003b). More general reviews of various earthquake location methods, including the noniterative/iterative algorithms (Ge 2003a,b) or the methods for single-event/multiple-event location (Thurber 2014), can be found in Ge (2003a,b) and Thurber (2014).

As discussed in many previous studies, the main factors determining the accuracy of earthquake location are the network geometry, measurement of phase arrival times, knowledge of background velocity model, and inversion algorithm (e.g. Waldhauser & Ellsworth 2000; Zhang *et al.* 2003; Schaff *et al.* 2004; Bondar *et al.* 2008; Maxwell *et al.* 2010). For the inversion algorithm, one of the key components is to accurately simulate seismic waves propagation (or at least predict the arrival times) in the given velocity model (e.g. Font *et al.* 2004; Chen *et al.* 2006). So far, most earthquake location methods are based on ray theory which assumes that traveltime and amplitude of an arrival only depend on (an)elastic properties along the geometrical ray path and ignores scattering, wave-front healing and other finite-frequency effects (e.g. Thurber 1985; Dahlen *et al.* 2000; Waldhauser & Ellsworth 2000; Zhang *et al.* 2003; Tong *et al.* 2011). However, seismic measurements such as traveltime and amplitude are sensitive to 3-D volumetric region off the ray path (e.g. Marquering *et al.* 1999; Dahlen *et al.* 2000; Tape *et al.* 2007). Furthermore, the ray theory is only valid when the scale length of the variation of material properties is much larger than the seismic wavelength (e.g. Rawlinson *et al.* 2010; Tong *et al.* 2014c,d). To accurately locate earthquakes, it is necessary to take into account the influence of off-ray structures by correctly capturing the interactions between the seismic waves and the potentially complex velocity model (e.g. Font *et al.* 2004; Liu *et al.* 2004). As pointed out by Tape *et al.* (2007) and Liu & Gu (2012), numerically solving the full wave equations is a promising approach to achieve this purpose. In the field of seismic tomography over the past decade, many high-resolution seismic images have been generated based upon numerical simulation of the full seismic wavefield, also known as full waveform inversion or adjoint tomogrpahy (e.g. Tape *et al.* 2009, 2010; Fichtner & Trampert 2011; Zhu *et al.* 2012; Rickers *et al.* 2013; Tong *et al.* 2014d). Generally speaking, the main advantages of numerically solving the full wave equations in seismic inverse problems are the freedom to choose either a 1-D or 3-D velocity model and the accurate calculation of synthetic seismograms and sensitivity kernels for complex models which may help generate more reliable images (Kim *et al.* 2011; Liu & Gu 2012; Tong *et al.* 2014b).

Based upon 3-D numerical wave simulations with the spectral-element solvers (e.g. Komatitsch & Tromp 1999; Komatitsch *et al.* 2004), Liu *et al.* (2004) and Kim *et al.* (2011) developed and implemented a moment tensor inversion procedure to obtain focal mechanisms, depths, and moment magnitudes of earthquakes. In this study, we only focus on earthquake location and intend to incorporate the advantages of numerical solutions to the full wave equations. For the sake of simplicity, we use a simple acoustic wave equation to approximate the wavefield. The Fréchet derivative of traveltime with respect to earthquake location is derived based on a different procedure from Liu *et al.* (2004) and Kim *et al.* (2011). We call the proposed method the acoustic wave-equation-based earthquake location method.

2 THEORY

An earthquake that occurred at the source location $\mathbf{x}_s$ is detected by a seismic station at $\mathbf{x}_r$. A perturbation $\delta \mathbf{m} = (\delta t_0, \delta \mathbf{x}_s)$ in earthquake location $\mathbf{m} = (t_0, \mathbf{x}_s)$ generally leads to a traveltime shift δt of a particular seismic phase at the receiver $\mathbf{x}_r$. As a perturbation δt_0 in earthquake origin time t_0 directly causes an arrival-time shift δt_0, only the traveltime shift $\delta t - \delta t_0$ caused by hypocentre perturbation $\delta \mathbf{x}_s$ is considered in the following discussion. We assume that $u(t, \mathbf{x}_r)$ and $s(t, \mathbf{x}_r)$ are the synthetic seismograms calculated with earthquake location parameters $\mathbf{m} = (t_0, \mathbf{x}_s)$ and $\mathbf{m} + \delta \mathbf{m} = (t_0, \mathbf{x}_s + \delta \mathbf{x}_s)$, respectively. If $|\delta \mathbf{m}| \ll |\mathbf{m}|$, we may expect that seismograms $u(t, \mathbf{x}_r)$ and $s(t, \mathbf{x}_r)$ are reasonably similar to each other. Based on this assumption, the traveltime shift $\delta t - \delta t_0$ of a particular phase can be calculated with high accuracy by maximizing the cross-correlation formula,

$$\max_{\delta t - \delta t_0} \frac{\int_0^T w(\tau) s(\tau, \mathbf{x}_r) u(\tau - (\delta t - \delta t_0), \mathbf{x}_r) d\tau}{\left[\int_0^T w(\tau) s^2(\tau, \mathbf{x}_r) d\tau \int_0^T w(\tau) u^2(\tau - (\delta t - \delta t_0), \mathbf{x}_r) d\tau \right]^{1/2}}, \tag{2}$$

where $w(t)$ is a time window function for isolating the interested seismic phase in the time interval $[0, T]$ (Tromp *et al.* 2005; Tong *et al.* 2014c). Based on the Born approximation (Dahlen *et al.* 2000), the maximum value of $\delta t - \delta t_0$ in eq. (2) can be alternatively computed via the following relationship

$$\delta t - \delta t_0 = \frac{1}{N_r} \int_0^T w(t) \frac{\partial u(t, \mathbf{x}_r)}{\partial t} [s(t, \mathbf{x}_r) - u(t, \mathbf{x}_r)] dt, \tag{3}$$
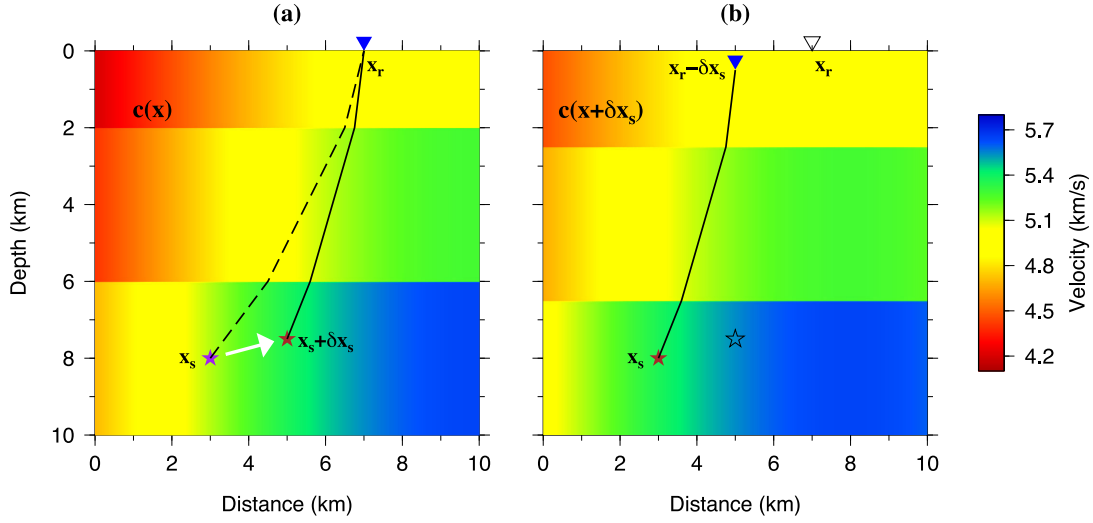
Figure 1. (a) Illustration of the initial hypocentre location $\mathbf{x}_s$, perturbated hypocentre location $\mathbf{x}_s + \delta\mathbf{x}_s$ and the receiver location $\mathbf{x}_r$ in the velocity model $c(\mathbf{x})$. Dashed and solid black curves denote the ray paths of the direct arrivals at $\mathbf{x}_r$ generated at $\mathbf{x}_s$ and $\mathbf{x}_s + \delta\mathbf{x}_s$, respectively. (b) An equivalent system in the velocity model $c(\mathbf{x} + \delta\mathbf{x}_s)$ for the perturbated hypocentre $\mathbf{x}_s + \delta\mathbf{x}_s$ and the receiver $\mathbf{x}_r$ in panel (a). Identical seismic waves are generated at $\mathbf{x}_s$ and recorded at $\mathbf{x}_r - \delta\mathbf{x}_s$. The black curve is the corresponding ray path of the direct arrival, same as the one in panel (a).

where

$$N_r = \int_0^T w(t) u(t, \mathbf{x}_r) \frac{\partial^2 u(t, \mathbf{x}_r)}{\partial t^2} \, dt.$$

2.1 Fréchet derivatives

We assume that seismic wave propagation with earthquake location parameter $\mathbf{m} = (t_0, \mathbf{x}_s)$ satisfies the acoustic wave equation

$$\begin{cases} \frac{\partial^2}{\partial t^2} u(t, \mathbf{x}) = \nabla \cdot \left[c^2(\mathbf{x}) \nabla u(t, \mathbf{x}) \right] + f(t - t_0) \delta(\mathbf{x} - \mathbf{x}_s), & \mathbf{x} \in \Omega, \\ u(0, \mathbf{x}) = \frac{\partial}{\partial t} u(0, \mathbf{x}) = 0, & \mathbf{x} \in \Omega, \\ \hat{\mathbf{n}} \cdot [c^2(\mathbf{x}) \nabla u(t, \mathbf{x})] = 0, & \mathbf{x} \in \partial\Omega, \end{cases} \tag{4}$$

where $u(t, \mathbf{x})$ is the displacement field, $c(\mathbf{x})$ represents the velocity distribution in the medium and $f(t)$ denotes the source time function (if $t \leq 0$ then $f(t) = 0$) at the source location $\mathbf{x}_s$. Similarly, displacement field $s(t, \mathbf{x}) = u(t, \mathbf{x}) + \delta u(t, \mathbf{x})$ for an earthquake with location parameter $\mathbf{m} + \delta\mathbf{m} = (t_0, \mathbf{x}_s + \delta\mathbf{x}_s)$ satisfies the following equation

$$\begin{cases} \frac{\partial^2}{\partial t^2} s(t, \mathbf{x}) = \nabla \cdot \left[c^2(\mathbf{x}) \nabla s(t, \mathbf{x}) \right] + f(t - t_0) \delta(\mathbf{x} - \mathbf{x}_s - \delta\mathbf{x}_s), & \mathbf{x} \in \Omega, \\ s(0, \mathbf{x}) = \frac{\partial}{\partial t} s(0, \mathbf{x}) = 0, & \mathbf{x} \in \Omega, \\ \hat{\mathbf{n}} \cdot [c^2(\mathbf{x}) \nabla s(t, \mathbf{x})] = 0, & \mathbf{x} \in \partial\Omega. \end{cases} \tag{5}$$

After a coordinate transformation from $\mathbf{x}$ to $\mathbf{x} + \delta\mathbf{x}_s$ (Alkhalifah 2010), it can be shown that seismic waves generated at hypocentre $\mathbf{x}_s + \delta\mathbf{x}_s$, propagated in the velocity model $c(\mathbf{x})$ and recorded at receiver $\mathbf{x}_r$ (Fig. 1a) are identical to the waves that are generated at $\mathbf{x}_s$, propagated in $c(\mathbf{x} + \delta\mathbf{x}_s)$ and recorded at $\mathbf{x}_r - \delta\mathbf{x}_s$ (Fig. 1b). The wavefield $p(t, \mathbf{x})$ in velocity model $c(\mathbf{x} + \delta\mathbf{x}_s)$ for a source at $\mathbf{x}_s$ can be described as

$$\begin{cases} \frac{\partial^2}{\partial t^2} p(t, \mathbf{x}) = \nabla \cdot \left[c^2(\mathbf{x} + \delta\mathbf{x}_s) \nabla p(t, \mathbf{x}) \right] + f(t - t_0) \delta(\mathbf{x} - \mathbf{x}_s), & \mathbf{x} \in \Omega, \\ p(0, \mathbf{x}) = \frac{\partial}{\partial t} p(0, \mathbf{x}) = 0, & \mathbf{x} \in \Omega, \\ \hat{\mathbf{n}} \cdot [c^2(\mathbf{x} + \delta\mathbf{x}_s) \nabla p(t, \mathbf{x})] = 0, & \mathbf{x} \in \partial\Omega. \end{cases} \tag{6}$$

The relationship between $s(t, \mathbf{x})$ and $p(t, \mathbf{x})$ is

$$s(t, \mathbf{x}) = p(t, \mathbf{x} - \delta\mathbf{x}_s) \approx p(t, \mathbf{x}) - \delta\mathbf{x}_s \cdot \nabla p(t, \mathbf{x}). \tag{7}$$

Clearly, the only difference between eqs (6) and (4) lies in a velocity perturbation $\delta\mathbf{x}_s \cdot \nabla c(\mathbf{x})$ from $c(\mathbf{x})$ in eq. (4) to $c(\mathbf{x} + \delta\mathbf{x}_s)$ in eq. (6), which accounts for the displacement perturbation $\delta u(t, \mathbf{x})$ from $u(t, \mathbf{x})$ to $p(t, \mathbf{x}) = u(t, \mathbf{x}) + \delta u(t, \mathbf{x})$. Subtracting eq. (4) from eq. (6) and

neglecting the second-order terms, we obtain

$$
\begin{cases}
\frac{\partial^2}{\partial t^2}\delta u(t,\mathbf{x}) = \nabla \cdot \left[c^2(\mathbf{x})\nabla\delta u(t,\mathbf{x}) + 2c(\mathbf{x})\delta\mathbf{x}_s \cdot \nabla c(\mathbf{x})\nabla u(t,\mathbf{x})\right], & \mathbf{x} \in \Omega, \\
\delta u(0,\mathbf{x}) = \frac{\partial}{\partial t}\delta u(0,\mathbf{x}) = 0, & \mathbf{x} \in \Omega, \\
\hat{\mathbf{n}} \cdot \left[c^2(\mathbf{x})\nabla\delta u(t,\mathbf{x}) + 2c(\mathbf{x})\delta\mathbf{x}_s \cdot \nabla c(\mathbf{x})\nabla u(t,\mathbf{x})\right] = 0, & \mathbf{x} \in \partial\Omega.
\end{cases}
\tag{8}
$$

Multiplying an arbitrary test function $q(t,\mathbf{x})$ on both sides of the first equation in eq. (8) and then integrating in the volume Ω and the time interval $[0, T]$, we have

$$
\int_0^T \mathrm{d}t \int_\Omega q(t,\mathbf{x})\frac{\partial^2}{\partial t^2}\delta u(t,\mathbf{x})\mathrm{d}\mathbf{x} = \int_0^T \mathrm{d}t \int_\Omega q(t,\mathbf{x})\nabla \cdot \left[c^2(\mathbf{x})\nabla\delta u(t,\mathbf{x}) + 2c(\mathbf{x})\delta\mathbf{x}_s \cdot \nabla c(\mathbf{x})\nabla u(t,\mathbf{x})\right]\mathrm{d}\mathbf{x}.
\tag{9}
$$

Integrating eq. (9) by parts gives

$$
\int_0^T \mathrm{d}t \int_\Omega \left\{\frac{\partial}{\partial t}\left[q(t,\mathbf{x})\frac{\partial}{\partial t}\delta u(t,\mathbf{x}) - \delta u(t,\mathbf{x})\frac{\partial}{\partial t}q(t,\mathbf{x})\right] + \delta u(t,\mathbf{x})\frac{\partial^2}{\partial t^2}q(t,\mathbf{x})\right\}\mathrm{d}\mathbf{x}
$$

$$
= \int_0^T \mathrm{d}t \int_\Omega \nabla \cdot \left\{q(t,\mathbf{x})\left[c^2(\mathbf{x})\nabla\delta u(t,\mathbf{x}) + 2c(\mathbf{x})\delta\mathbf{x}_s \cdot \nabla c(\mathbf{x})\nabla u(t,\mathbf{x})\right]\right\}\mathrm{d}\mathbf{x}
$$

$$
- \int_0^T \mathrm{d}t \int_\Omega \nabla \cdot \left[\delta u(t,\mathbf{x})c^2(\mathbf{x})\nabla q(t,\mathbf{x})\right]\mathrm{d}\mathbf{x} + \int_0^T \mathrm{d}t \int_\Omega \delta u(t,\mathbf{x})\nabla \cdot \left[c^2(\mathbf{x})\nabla q(t,\mathbf{x})\right]\mathrm{d}\mathbf{x}
$$

$$
- \int_0^T \mathrm{d}t \int_\Omega 2c(\mathbf{x})\delta\mathbf{x}_s \cdot \nabla c(\mathbf{x})\nabla q(t,\mathbf{x}) \cdot \nabla u(t,\mathbf{x})\,\mathrm{d}\mathbf{x}.
\tag{10}
$$

If relationship (7) is substituted into eq. (3), then the traveltime shift $\delta t - \delta t_0$ can be expressed as

$$
\delta t - \delta t_0 = \frac{1}{N_r}\int_0^T w(t)\frac{\partial u(t,\mathbf{x}_r)}{\partial t}\delta u(t,\mathbf{x}_r)\mathrm{d}t - \frac{1}{N_r}\int_0^T w(t)\frac{\partial u(t,\mathbf{x}_r)}{\partial t}\delta\mathbf{x}_s \cdot \nabla u(t,\mathbf{x}_r)\mathrm{d}t.
\tag{11}
$$

Then by adding up eqs (10) and (11), using initial and boundary conditions in eq. (8), and assuming that the auxiliary field $q(t,\mathbf{x})$ satisfies the following wave equation

$$
\begin{cases}
\frac{\partial^2}{\partial t^2}q(t,\mathbf{x}) - \nabla \cdot \left[c^2(\mathbf{x})\nabla q(t,\mathbf{x})\right] = \frac{1}{N_r}w(t)\frac{\partial u(t,\mathbf{x})}{\partial t}\delta(\mathbf{x}-\mathbf{x}_r), & \mathbf{x} \in \Omega, \\
q(T,\mathbf{x}) = \partial q(T,\mathbf{x})/\partial t = 0, & \mathbf{x} \in \Omega, \\
\hat{\mathbf{n}} \cdot c^2(\mathbf{x})\nabla q(t,\mathbf{x}) = 0, & \mathbf{x} \in \partial\Omega,
\end{cases}
\tag{12}
$$

we obtain the relationship for traveltime shift as

$$
\delta t - \delta t_0 = -\delta\mathbf{x}_s \cdot \frac{1}{N_r}\int_0^T w(t)\frac{\partial u(t,\mathbf{x}_r)}{\partial t}\nabla u(t,\mathbf{x}_r)\,\mathrm{d}t
$$

$$
- \delta\mathbf{x}_s \cdot \int_0^T \mathrm{d}t \int_\Omega 2c(\mathbf{x})\nabla c(\mathbf{x})\nabla q(t,\mathbf{x}) \cdot \nabla u(t,\mathbf{x})\,\mathrm{d}\mathbf{x}.
\tag{13}
$$

Define the Fréchet derivative $\mathbf{G} = \left(G_{t_0}, \mathbf{G}_{\mathbf{x}_s}\right)$ with respect to the origin time t_0 and hypocentre location $\mathbf{x}_s$ as

$$
G_{t_0}(\mathbf{x};\mathbf{x}_r,\mathbf{x}_s) = 1,
\tag{14}
$$

$$
\mathbf{G}_{\mathbf{x}_s}(\mathbf{x};\mathbf{x}_r,\mathbf{x}_s) = (G_x, G_y, G_z) = -\frac{1}{N_r}\int_0^T w(t)\frac{\partial u(t,\mathbf{x}_r)}{\partial t}\nabla u(t,\mathbf{x}_r)\,\mathrm{d}t
$$

$$
- \int_0^T \mathrm{d}t \int_\Omega 2c(\mathbf{x})\nabla c(\mathbf{x})\nabla q(t,\mathbf{x}) \cdot \nabla u(t,\mathbf{x})\,\mathrm{d}\mathbf{x},
\tag{15}
$$

we can obtain the following relationship which links the traveltime shift δt and the earthquake location perturbation $\boldsymbol{\delta m} = (\delta t_0, \delta\mathbf{x}_s) = (\delta t_0, \delta x, \delta y, \delta z)$ as

$$
\delta t = \mathbf{G}\delta\mathbf{m} = G_{t_0}\delta t_0 + \mathbf{G}_{\mathbf{x}_s} \cdot \delta\mathbf{x}_s = G_{t_0}\delta t_0 + G_x\delta x + G_y\delta y + G_z\delta z.
\tag{16}
$$

The relationship (16) is similar to Geiger's method as shown in eq. (1), except that we need to solve two wave equations (4) and (12) to calculate the Fréchet derivatives in eq. (15) instead of tracing the ray path.

2.2 Inverse problem

For a particular seismic phase (such as direct *P*-wave or *S*-wave) generated by an event initially assumed at $\mathbf{m} = (t_0, \mathbf{x}_s)$, usually some time-shifts $\mathbf{d} = (\delta t_i)_{N \times 1}$ can be measured at N seismic stations between the observed arrival times and the theoretical arrival times calculated in the known velocity model $c(\mathbf{x})$. If the observing errors $\mathbf{e} = (e_i)_{N \times 1}$ are taken into account, we have a concise matrix form for determining the earthquake location perturbation $\delta \mathbf{m} = (\delta t_0, \delta \mathbf{x}_s)$ as

$$\mathbf{d} = \mathbf{G}\delta\mathbf{m} + \mathbf{e} \tag{17}$$

where $\mathbf{G}$ is an $N \times 4$ sensitivity matrix with entries g_{ij}. Here, g_{ij} ($j = 1, 2, 3, 4$) are (G_{t_0}, G_x, G_y, G_z) in eq. (16) related to the ith observation. The standard damped least-squares solution for equation (17) with the minimum norm constraint is given by

$$\delta\mathbf{m} = (\mathbf{G}^T\mathbf{G} + \lambda\mathbf{I})^{-1}\mathbf{G}^T(\mathbf{d} - \mathbf{e}), \tag{18}$$

where I is a 4×4 identity matrix; λ is a non-negative damping parameter specified prior to the inversion to provide the intended weight of the minimum norm criterion. Once the earthquake location perturbation $\boldsymbol{\delta}\,\mathbf{m}$ is obtained, we can have an updated earthquake location $\mathbf{m} + \boldsymbol{\delta}\,\mathbf{m}$. Usually, an iterative procedure is needed to get an accuracy earthquake location. We call the whole process of calculating the Fréchet derivatives in eq. (16) and solving eq. (18) to obtain the final earthquake location 'the acoustic wave-equation-based earthquake location'.

2.3 Discussion on the Fréchet derivative $\mathbf{G}_{\mathbf{x}_s}(\mathbf{x}; \mathbf{x}_r, \mathbf{x}_s)$

The traveltime derivative $\mathbf{G}_{\mathbf{x}_s}(\mathbf{x}; \mathbf{x}_r, \mathbf{x}_s)$ in eq. (15) with respect to the hypocentre position $\mathbf{x}_s$ consists of two terms $\mathbf{G}_{\mathbf{x}_s}^1$ and $\mathbf{G}_{\mathbf{x}_s}^2$ as

$$\mathbf{G}_{\mathbf{x}_s}^1 = -\frac{1}{N_r}\int_0^T w(t)\frac{\partial u(t, \mathbf{x}_r)}{\partial t}\nabla u(t, \mathbf{x}_r)\,\mathrm{d}t \tag{19}$$

and

$$\mathbf{G}_{\mathbf{x}_s}^2 = -\int_0^T \mathrm{d}t \int_\Omega 2c(\mathbf{x})\nabla c(\mathbf{x})\nabla q(t, \mathbf{x}) \cdot \nabla u(t, \mathbf{x})\,\mathrm{d}\mathbf{x}. \tag{20}$$

Generally speaking, $\mathbf{G}_{\mathbf{x}_s}^1$ mainly accounts for the influence caused by the geometrical mislocation of the hypocentre (zeroth-order influence), while $\mathbf{G}_{\mathbf{x}_s}^2$ considers the impact of the spatial variation of the velocity model (first-order influence). For example, if the hypocentre moves closer to the receiver, $\mathbf{G}_{\mathbf{x}_s}^1$ indicates that the traveltime should be reduced. But even if the hypocentre is closer to the receiver, it is possible that the considered seismic phase may pass through a region with a lower velocity structure. In this case, $\mathbf{G}_{\mathbf{x}_s}^2$ suggests an increase in traveltime. Specifically, we consider a homogeneous model with constant velocity c. Assuming that an impulsive source $f(t) = \delta(t - t_0)$ is exerted at the source, the wavefield recorded at $\mathbf{x}_r$ has an analytical form as $u(t, \mathbf{x}_r) = \delta(t - t_0 - |\mathbf{x}_r - \mathbf{x}_s|/c)/(4\pi|\mathbf{x}_r - \mathbf{x}_s|)$, and the first term in eq. (15) is simplified to $\mathbf{G}_{\mathbf{x}_s}^1 = -(\mathbf{x}_r - \mathbf{x}_s)/(c|\mathbf{x}_r - \mathbf{x}_s|)$ and the second term $\mathbf{G}_{\mathbf{x}_s}^2$ vanishes. $\mathbf{G}_{\mathbf{x}_s}^1$ is the same as the derivative of arrival time with respect to the hypocentre location as shown in eq. (1), which is derived in the framework of ray theory (Geiger 1910; Engdahl & Lee 1976; Thurber 2014). That is to say, $\mathbf{G}_{\mathbf{x}_s}^1$ can be roughly considered as the Fréchet derivatives described in Geiger's method for a homogeneous model; and the other term $\mathbf{G}_{\mathbf{x}_s}^2$ additionally takes into account the velocity variation, which could be helpful for earthquake location in complex media.

Sensitivity or Fréchet kernels defined as the volumetric densities of the Fréchet derivative are widely used in tomographic studies of volumetric material properties (e.g. Dahlen *et al.* 2000; Tromp *et al.* 2005; Fichtner & Trampert 2011; Tong *et al.* 2014a). They have direct physical meanings in interpreting the finite-frequency effects of propagating seismic waves. Based on $\mathbf{G}_{\mathbf{x}_s}^2$ in eq. (20), we can also introduce sensitivity or Fréchet kernel for earthquake location as

$$\mathbf{K}_{\mathbf{x}_s} = (K_x, K_y, K_z) = -\int_0^T 2c(\mathbf{x})\nabla c(\mathbf{x})\nabla q(t, \mathbf{x}) \cdot \nabla u(t, \mathbf{x})\,\mathrm{d}t. \tag{21}$$

The velocity model $c(\mathbf{x})$ and its spatial variation $\nabla c(\mathbf{x})$, the distribution of the hypocentre $\mathbf{x}_s$ and receiver $\mathbf{x}_r$, and the considered seismic phase together determine the sensitivity kernel (21) in earthquake location inversion. Note that the Fréchet kernel for earthquake location is simply multiplying $\nabla c(x)$ to the volumetric sensitivity kernel for c($\mathbf{x}$) in tomographic inversions (Tong *et al.* 2014d).

2.4 2-D forward modelling and 3-D inversion

It is known that seismic tomography based on the simulation of full wavefield is computationally expensive (e.g. Chen *et al.* 2007; Tape *et al.* 2009; Zhu *et al.* 2012; Tong *et al.* 2014d). Since two wave equations need be solved to obtain the Fréchet derivative, the acoustic wave-equation-based earthquake location method developed in this study is also computationally demanding, especially when 3-D spatial geometry is considered. To reduce the computational cost, following the approximation technique used in wave-equation-based traveltime seismic tomography (Tong *et al.* 2014c,d), we suggest to restrict the simulation of wavefield in a 2-D vertical plane passing through the hypocentre and receiver. The horizontal direction from the hypocentre to receiver is defined as r. The angle between r and the x-axis is θ. Within the 2-D vertical plane, the traveltime Fréchet derivative with respect to the hypocentre location $\mathbf{x}_s$ has two components $\mathbf{G}_{\mathbf{x}_s} = (G_r, G_z)$. To invert for 3-D earthquake location, we can further project the component G_r onto two horizontal directions as $(G_x, G_y) = (G_r\cos\theta, G_r\sin\theta)$.
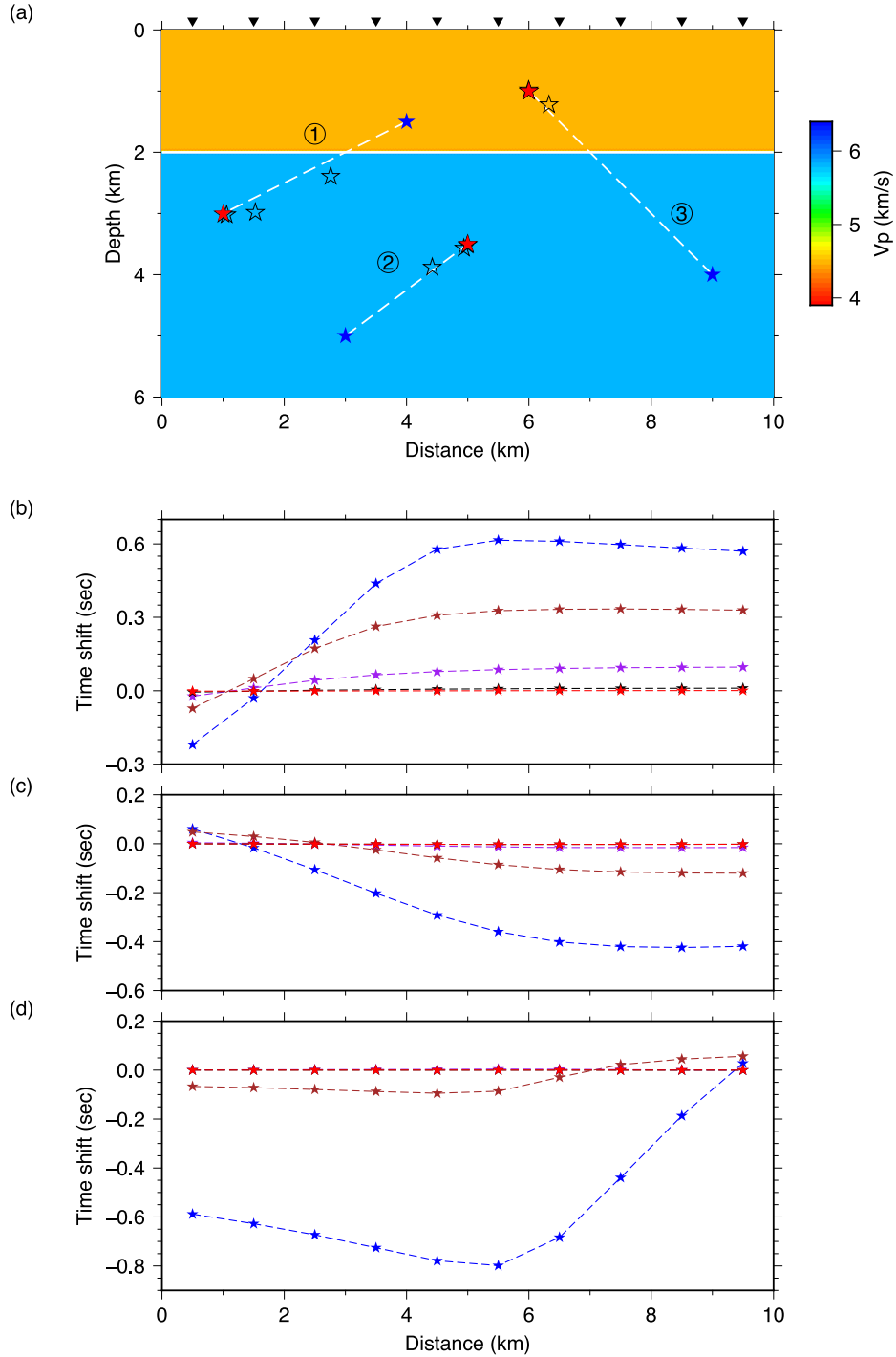
Figure 2. (a) The three different cases of earthquake location. The blue stars are the initial locations of the three earthquakes, the red stars are the 'true' locations and the black empty stars denote the iteratively updated locations. (b–d) The *P*-wave traveltime residuals calculated at each station with iteratively updated earthquake locations. The blue, brown, purple, black and red stars connected with dashed curves are the traveltime residuals calculated at the initial, 1st, 2nd, 3rd, 4th and 5th locations, respectively. (b), (c) and (d) are corresponding to the 1st, 2nd, and 3rd cases discussed in the main text, respectively.

In this scenario, the linearized relationship between traveltime perturbation and earthquake location perturbation shown in eq. (16) can be modified into

$$\delta t = \mathbf{G}\delta \mathbf{m} = G_{t_0}\delta t_0 + \mathbf{G}_{\mathbf{x}_s}\delta \mathbf{x}_s = G_{t_0}\delta t_0 + \cos\theta\, G_r \delta x + \sin\theta\, G_r \delta y + G_z \delta z. \tag{22}$$

Eq. (22) only requires the simulation of full wavefield in a 2-D vertical plane but can be used to invert for 3-D earthquake location. This 2.5-D strategy is computationally more efficient compared to the one based on 3-D forward modelling.

Table 1. The earthquake location throughout the iteration corresponding to the first case in Fig. 2(a).

	Initial	1st	2nd	3rd	4th	Target
x (km)	4.0	2.7580	1.5262	1.0579	1.0049	1.0
z (km)	1.5	2.3941	2.9817	3.0219	3.0092	3.0
t_0 (s)	0.0	0.1877	0.0855	0.0054	−0.0010	0.0

Table 2. The same as Table 1 but for the second case in Fig. 2(a).

	Initial	1st	2nd	3rd	4th	Target
x (km)	3.0	4.4208	4.9359	4.9942	4.9998	5.0
z (km)	5.0	3.8777	3.5672	3.5155	3.5034	3.5
t_0 (s)	0.0	0.0082	−0.0010	−0.0023	−5.4325e−04	0.0

3 NUMERICAL EXAMPLES

We test the performances of the acoustic wave-equation-based earthquake location method with four synthetic numerical examples.

3.1 The two-layer model

We first consider a two-layer velocity model (Fig. 2a). For demonstration purpose, only 2-D geometries are considered in this and the next proof-of-concept examples. The implementation of the proposed earthquake location method in 3-D geometries is very similar. As an attempt to fully demonstrate the performances of the new earthquake location method, three different cases are discussed: (1) The initial hypocentre location is in the top layer, but the true location is in the bottom layer. (2) Both initial and actual hypocentre locations are in the bottom layer. (3) The initial location is in the bottom layer, while the true location is in the top layer (Fig. 2a). The origin time is not perturbed but iteratively updated in this example. Ten seismic stations with an equal spacing of 1.0 km are employed at the surface to record seismograms generated

Table 3. The same as Table 1 but for the third case in Fig. 2(a).

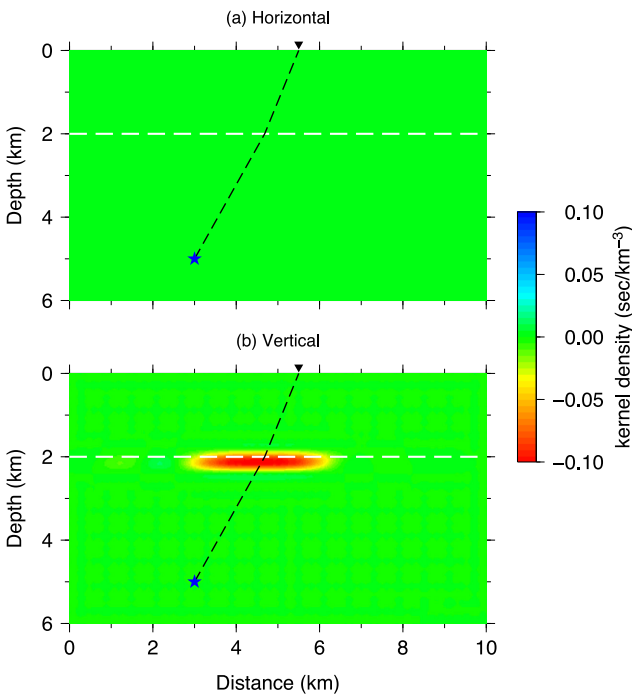|	Initial	1st	2nd	3rd	4th	Target
x (km)	9.0	6.3286	5.9958	5.9958	6.0001	6.0
z (km)	4.0	1.2215	0.9834	1.0027	0.9999	1.0
t_0 (s)	0.0	0.3433	7.8780e−06	3.2683e−04	−7.0075e−05	0.0

Figure 3. (a) The horizontal and (b) vertical components of the Fréchet kernel $\mathbf{K}_{\mathbf{x}_s}$ in eq. (21) corresponding to the earthquake in the bottom layer (blue star) and the receiver on the surface (black inverse triangle).

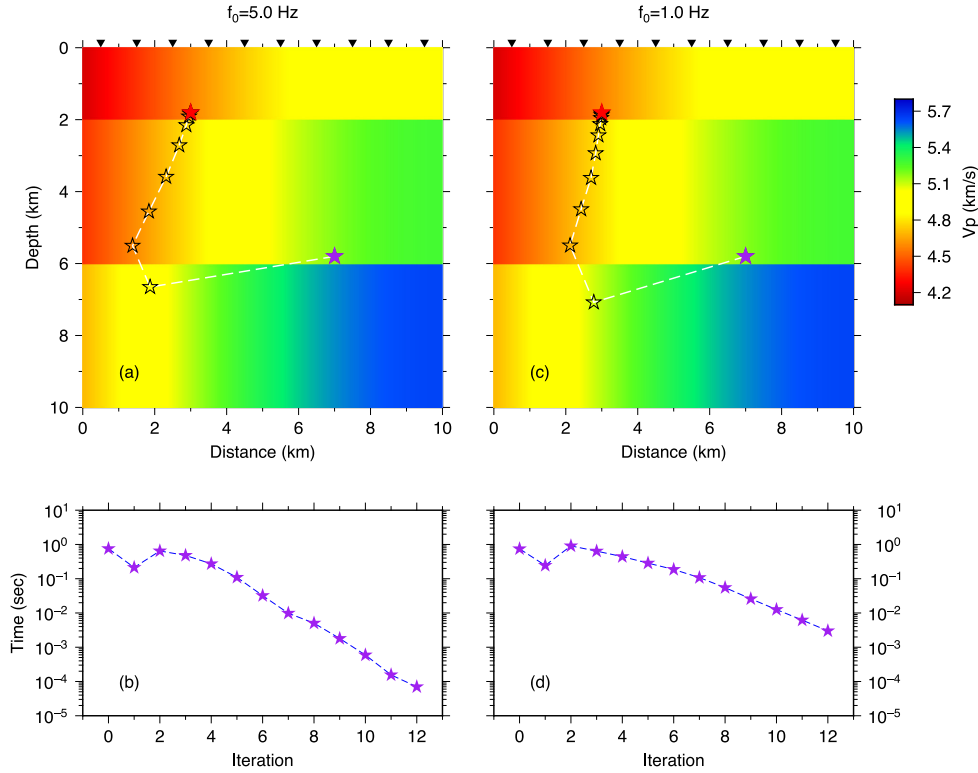**Figure 4.** The iteratively updated earthquake location (a,c) and the root mean square of the first *P*-wave traveltime residuals (b,d). The purple, black empty and red stars are the initial, intermediate and 'targeted' hypocentre locations. (a,b) are obtained with the high-frequency ($f_0 = 5.0$ Hz) data, while (c,d) are the results of the low-frequency ($f_0 = 1.0$ Hz) data.

Table 4. The earthquake locations throughout the iteration by inverting the high-frequency ($f_0 = 5.0$ Hz) data.

	Initial	1st	2nd	3rd	4th	6th	8th	10th	12th	Target
x (km)	7.0	1.8716	1.3824	1.8383	2.3166	2.8744	2.9873	2.9986	2.9998	3.0
z (km)	5.8	6.6524	5.5040	4.5522	3.5872	2.1526	1.8362	1.8039	1.8004	1.8
t_0 (s)	0.0	−0.5104	−0.6791	−0.4908	−0.2866	−0.0404	−0.0052	−0.00057	−0.00006	0.0

at the initial, iteratively updated and actual earthquake locations. In this study, only the first *P*-wave arrivals are used to locate the earthquakes and all the synthetic seismograms are generated with a Ricker wavelet point source $f(t - t_0)$ in eq. (4) which has an analytical form of

$$f(t - t_0) = A \left[1 - 2\pi^2 f_0^2 (t - t_0)^2 \right] \exp \left[-\pi^2 f_0^2 (t - t_0)^2 \right]. \tag{23}$$

f_0 is the dominant frequency chosen as $f_0 = 1.0$ Hz here and A is the normalization factor. A high-order finite-difference method is adopted to simulate the full wavefields (Tong *et al.* 2014c).

Fig. 2(a) and Tables 1–3 show the iteratively updated earthquake locations. The corresponding traveltime residuals of the first *P*-arrivals at each station are shown in Figs 2(b)–(d). We can observe that the acoustic wave-equation-based earthquake location method can accurately locate the three earthquakes after about 4 iterations, showing the validity of this new technique. To examine the effect of velocity variation on earthquake location, we calculate and show one Fréchet kernel $\mathbf{K}_{\mathbf{x}_s}$ in Fig. 3. Since the velocity model has no lateral variation, the horizontal component of $\mathbf{G}_{\mathbf{x}_s}^2$ is zero. Meanwhile, the vertical component of $\mathbf{G}_{\mathbf{x}_s}^2$ reflects the influence of the velocity discontinuity on locating the depth of the earthquake.

3.2 Inversion with seismic data of different frequencies

As discussed previously, the acoustic wave-equation-based earthquake location method naturally takes into account the finite-frequency effects of the seismic waves. In the second example, we explore the influence of different frequency contents of seismic waves on the accuracy of earthquake location in a 3-layer velocity model with lateral variation (Fig. 4). The hypocentre is actually located in the top layer but initially assumed to be near the bottom of the middle layer (Fig. 4). We use the first *P*-waves at dominant frequencies $f_0 = 5.0$ Hz and $f_0 = 1.0$ Hz to locate this earthquake separately. Fig. 4 shows the iteratively updated hypocentre locations and the corresponding root mean square (RMS) of the first *P*-wave traveltime residuals. Tables 4 and 5 quantitatively demonstrate the earthquake location throughout the iterations for using the high-frequency and low-frequency data, respectively. Generally speaking, using both high- and low-frequency seismic data can accurately locate the earthquake with the acoustic wave-equation-based earthquake location method. But a closer examination reveals

Table 5. The same as Table 4 but with low-frequency ($f_0 = 1.0$ Hz) data.

	Initial	1st	2nd	3rd	4th	6th	8th	10th	12th	Target
x (km)	7.0	2.7790	2.1191	2.4261	2.7018	2.9063	2.9809	2.9963	2.9991	3.0
z (km)	5.8	7.0784	5.4980	4.4896	3.6197	2.4361	1.9562	1.8368	1.8089	1.8
t_0 (s)	0.0	−0.5391	−0.7878	−0.5512	−0.3682	−0.1414	−0.0390	−0.0090	−0.0021	0.0

that higher-frequency seismic data can locate the earthquake more precisely. For example, after 12 iterations the RMS of the first *P*-wave traveltime residuals is in the order of 10^{-4} s (Fig. 4c) and 10^{-3} s (Fig. 4d) for the high- and low-frequency cases, respectively. Tables 4 and 5 also indicate that higher-frequency data can find a closer earthquake location to the 'true' location after the same number of iterations. Fig. 5 displays the sensitivity kernels for the horizontal location and depth, which are corresponding to a single source–receiver pair. The obvious observation is that the high-frequency data have a smaller influence zone (sensitivity kernel with nontrivial value) than the low-frequency data do. That is to say, different frequency components of the same seismic phase may have slightly different arriving times if the velocity model has spatial variation. This also suggests that we need to consider both the finite-frequency effects of the propagating seismic waves and the velocity variation for accurate earthquake locations as the proposed acoustic wave-equation-based technique does.

3.3 Earthquake location with the 2.5-D approach

Previous numerical examples have verified the concept of acoustic wave-equation-based earthquake location in 2-D geometries. In Section 2, we also proposed to use a 2.5-D approach to locate earthquakes in 3-D space with 2-D forward modellings to reduce the computational cost. The third example is designed to test this 2.5-D approach in an extreme case. The considered velocity model consists of the crust and the mantle, containing an undulated Moho and a subduction zone with a thin low velocity layer atop a fast velocity layer (Fig. 6). The central part of the Moho has a maximum elevation of 10.0 km from the flat position at the depth of 30.0 km. Comparing to the surrounding mantle, the velocities of the fast and slow velocity layers of the subduction zone are perturbed by +4 per cent and −6 per cent, respectively. The initial hypocentre location of the earthquake is in the high velocity layer of the subduction zone, about 115 km away from the 'true' location in the above low velocity zone (Fig. 6). The origin time of the earthquake is also delayed by 5.0 s from the 'actual' origin time. Three arrays of and a total of 21 seismic stations on the surface are used to record seismograms (Fig. 6). The dominant frequency of all the seismograms is
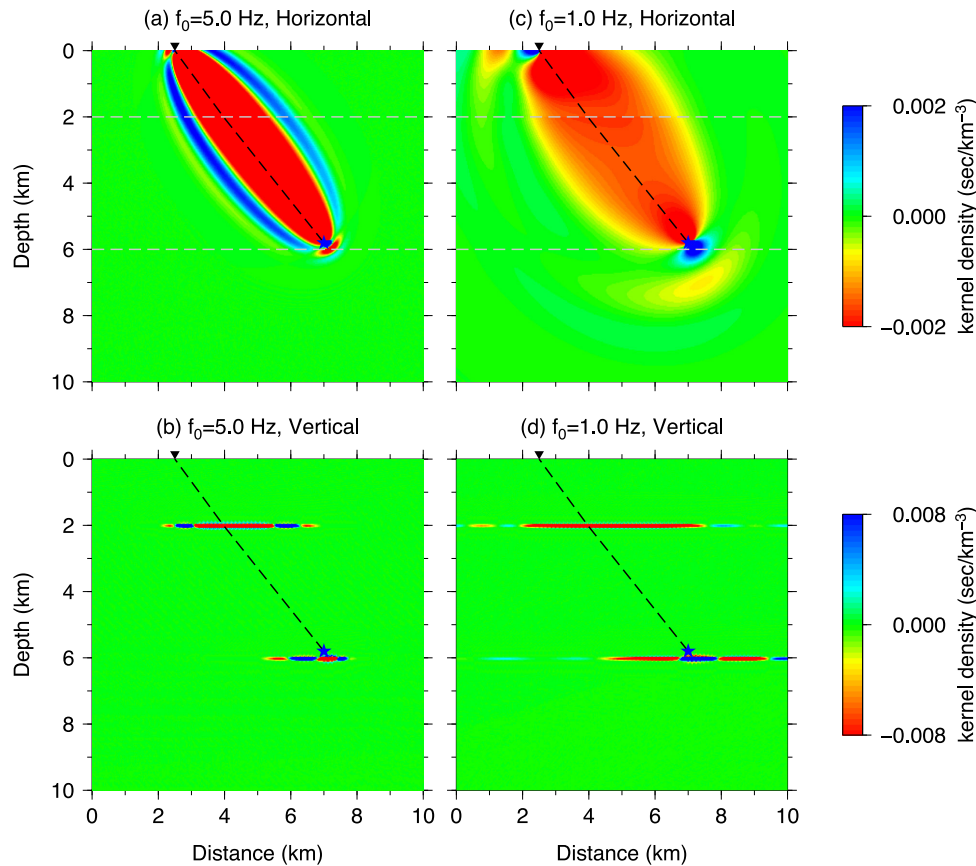

Figure 5. (a,c) The horizontal and (b,d) vertical components of the Fréchet kernel in eq. (21) calculated at the initial earthquake location near the bottom of the middle layer. (a,b) are the high-frequency sensitivity kernels, and (c,d) are the low-frequency kernels.
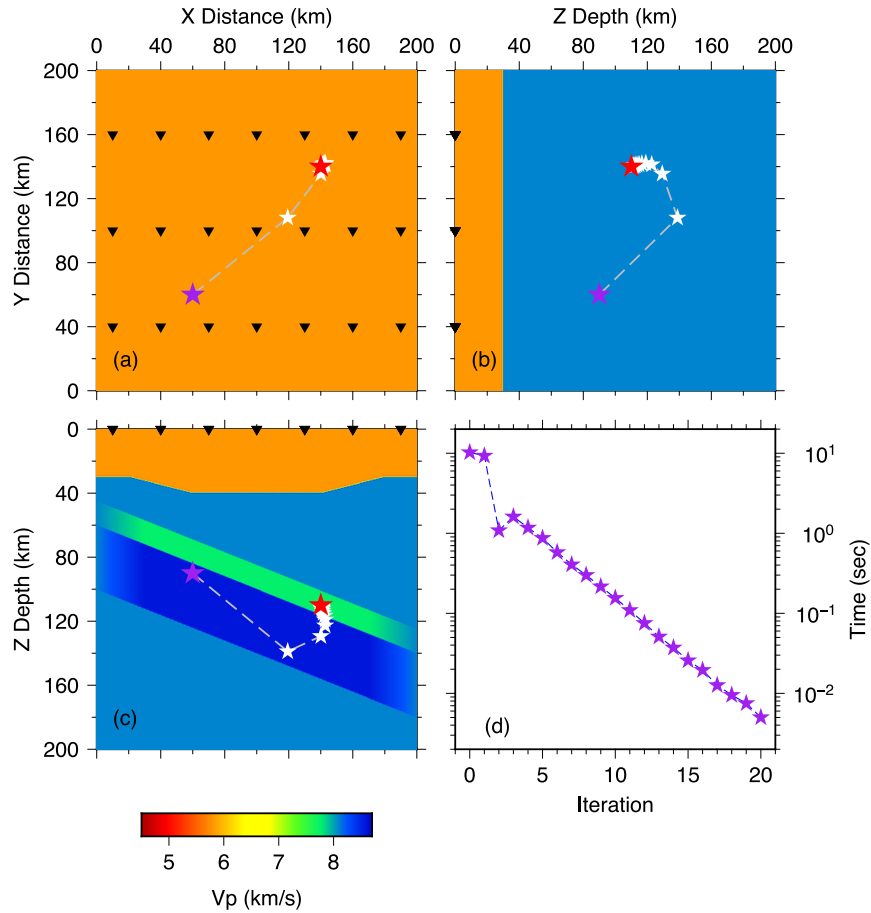
Figure 6. (a–c) Three different planar views of the velocity model and the spatial distributions of the initial, actual and iteratively updated earthquake locations. The purple, white and red stars represent the initial, iteratively updated and the 'targeted' hypocentre locations, respectively. The black inverse triangles are the seismic stations. (d) The root mean square of the traveltime residuals of the first *P*-arrivals throughout the iteration.

Table 6. The iteratively updated earthquake location obtained by using the 2.5-D approach in a crust-over-mantle model with an undulated Moho and a subduction zone (Fig. 6).

	Initial	1st	2nd	3rd	6th	10th	15th	19th	20th	Target
x (km)	60.	119.37	140.05	142.75	141.50	140.44	140.08	140.01	140.01	140.
y (km)	60.	108.10	135.51	141.36	141.42	140.40	140.07	140.02	140.02	140.
z (km)	90.	138.83	129.31	122.72	114.90	111.19	110.19	110.05	110.05	110.
t_0 (s)	5.	3.8370	−1.2160	−1.4014	−0.5466	−0.1441	−0.0240	−0.0063	−0.0050	0.

$f_0 = 0.2$ Hz. Fig. 6 displays the iteratively relocated hypocentre locations (Figs 6a–c) and the corresponding root mean square values of the first *P*-wave traveltime residuals (Fig. 6d). Meanwhile, Table 6 quantitatively demonstrates the initial, updated, and target earthquake locations. The hypocentre location and origin time errors at the 20th iteration are less than 0.06 km and 0.005 s, respectively. The errors are mainly caused by the comparatively large grid interval (1.0 km) used in the forward modelling scheme, the numerical wave-equation solver itself, and the resolving ability of the relatively low frequency ($f_0 = 0.2$ Hz) data. All the results of this example indicate that the 2.5-D version of the acoustic wave-equation-based earthquake location method can accurately locate the earthquake even though the initial location is far away from the 'true' location.

3.4 Influence of inaccurate velocity model

The accuracy of earthquake location relies on how well we know the velocity model. Since the 'exact' velocity model is always not available, we should bear in mind that earthquake locations are usually obtained by using approximate velocity models in real applications. All the previous examples reveal that the acoustic wave-equation-based earthquake location method has excellent performance in locating earthquakes if the known velocity models are exactly the ones in which the data are generated. To investigate our technique for locating real earthquakes, in the fourth example we test the performance of the 2.5-D version of the proposed method when only an approximate model is provided.

For a direct comparison purpose, we relocate the earthquake discussed in the third example again. All the parameters are the same except that the velocity structure for generating synthetic seismograms is simplified into a two-layer model with a flat Moho at the depth
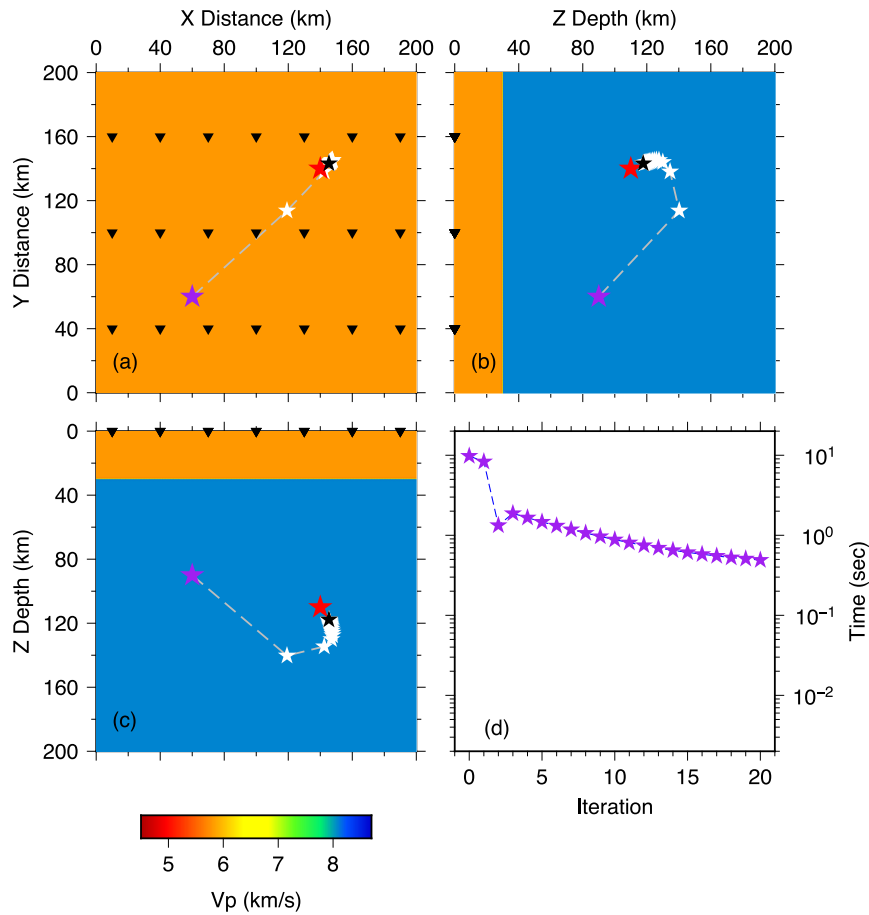
Figure 7. The same as Fig. 6 but a simple and approximate crust-over-mantle model with a flat Moho is used for earthquake location. In panels (a)–(c), the black stars are the 20th hypocentre location which is considered to be the final result of the acoustic wave-equation-based earthquake location.

of 30.0 km (Fig. 7). Note that the data generated at the 'true' earthquake location is still calculated in the 'true' velocity model as that of Figs 6(a)–(c). The iteratively updated earthquake locations relocated in the simple two-layer velocity model are shown in Fig. 7 and Table 7. After 20 iterations, the inverted earthquake location is close to the 'actual' location but there is still an obvious gap between them (Fig. 7). Table 7 reveals that the final spatial location error is about 10.0 km, though it is much smaller than the initial location error of 115.0 km. Specifically, the earthquake depth is 7.73 km deeper than the real depth and the origin time t_0 is advanced by 0.48 s in contrast to initially being delayed by 5.0 s. Comparing the 'true' and 'approximate' velocity models suggests that the velocity model used for earthquake location does not account for the crustal low velocity structure below 30.0 km and the low velocity layer of the subducting slab. The failure of considering these low velocity structures makes the earthquake deeper. This example indicates that relocating earthquakes in approximate velocity models is likely to obtain approximate earthquake locations with the acoustic wave-equation-based earthquake location method.

4 REAL DATA APPLICATION

The main purpose of developing the acoustic wave-equation-based earthquake location method is to use it to locate earthquakes in real applications. Liu *et al.* (2004) proposed a moment tensor inversion procedure based upon spectral-element simulations and obtained focal mechanisms, depths, and moment magnitudes of three southern California earthquakes including the 2004 M_L 5.4 Big Bear event (Fig 8a). They claimed that their inversion results are generally in good agreement with estimates based upon traditional body-wave and surface-wave inversions (Liu *et al.* 2004). In this study, we also choose the 2004 Big Bear earthquake as the test event to further explore our new 2.5-D earthquake location method.

Table 7. The same as Table 6 but the results are obtained in a simple crust-over-mantle model (Fig. 7).

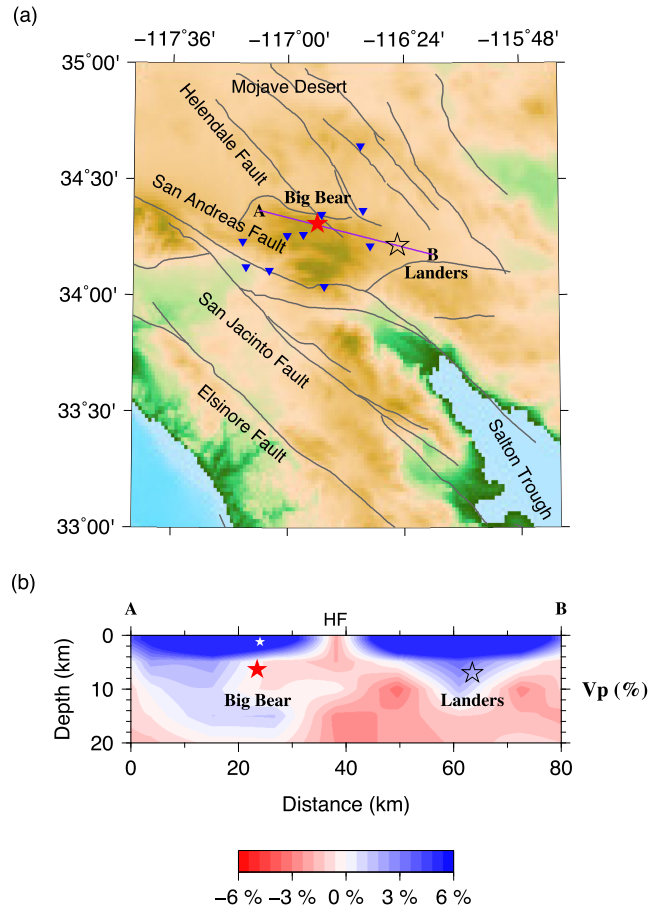|	Initial	1st	2nd	3rd	6th	10th	15th	19th	20th	Target
x (km)	60.	119.17	142.47	147.02	147.23	146.29	145.69	145.45	145.42	140.
y (km)	60.	113.71	138.13	144.05	145.07	144.11	143.49	143.25	143.20	140.
z (km)	90.	140.24	134.54	130.00	124.68	121.05	118.76	117.89	117.73	110.
t_0 (s)	5.	3.3118	−1.5483	−1.8007	−1.2837	−0.8616	−0.5964	−0.4948	−0.4772	0.

(a)

(b)

Figure 8. (a) The tectonic conditions and surface topography around the 2004 Big Bear earthquake (red star) area. The inverted blue stars are 10 seismic stations. Seismic data recorded by these stations are used to locate the Big Bear earthquake. The empty black star represents the 1992 M_w 7.3 Landers earthquake. The grey curves are active faults. Profile AB crosses the epicentres of the 2004 Big Bear earthquake and the 1992 Landers earthquake. (b) *P*-wave velocity structure along Profile AB in panel (a) down to the depth of 20 km. The Vp structure is recovered by Tong *et al.* (2014d). The white and red stars denote the initial and final locations of the Big Bear event, respectively. Blue and red colours indicate high- and low-velocity structures as shown in the colour bar.

We download broadband seismic data from Southern California Seismic Network (http://scsn.org). Only the first *P*-waves recorded at the 10 nearest seismic stations are used to locate the 2004 Big Bear earthquake. All the 10 seismic stations are at epicentral distances less than 45 km (Fig. 8a). The earthquake location is conducted in a 1-D layered model, which is separated by discontinuities at the depths of 5.5, 16.0 and 29.2 km (Tong *et al.* 2014d). The *P*-wave velocities in the four layers are 5.5, 6.3, 6.7 and 7.8 km s^{-1}, respectively. The dominant frequency of the source time function (23) is chosen as $f_0 = 1.0$ Hz. As a result, the nontrivial part of each synthetic seismogram lasts for nearly 2.0 s (twice the dominant period). To be consistent, 2-s time windows starting at the picked onset times of the *P*-arrivals (from the SCSN catalogue) are used to isolate the portions of the data for earthquake location. A Butterworth filter between 0.1 and 1.3 Hz is then applied to the windowed seismograms. For effectively measuring the cross-correlation traveltime residuals between the synthetics and observed data, all the 2-D waveforms are converted to 3-D seismograms using the conversion formula derived in Miksat *et al.* (2008). We relocate the Big Bear earthquake starting from its SCSN catalogue location. Similar to Liu *et al.* (2004), the origin time of the earthquake is fixed and only the hypocentre location is updated in this test.

Table 8 contains the iteratively inverted hypocentre locations and the corresponding RMS values of the first *P*-wave traveltime residuals. We can observe that the lateral location (Longitude, Latitude) of the Big Bear earthquake has very small variations but the depth becomes deeper by more than 5.0 km throughout a total of 14 iterations. The RMS value of the traveltime residuals is reduced from 0.33 to 0.15 s with a minimum value of 0.13 s at the first iteration. Although the RMS value reaches a minimum after a single iteration, we do not stop the relocation procedure because the earthquake location still varies significantly in the following iterations. After 14 iterations, we almost obtain a stable solution and consider it as the final earthquake location of the Big Bear event. Using three different inversion schemes including the spectral-element moment tensor inversion, Liu *et al.* (2004) concluded that the depth of the 2004 Big Bear earthquake is about 6.4 ± 0.2 km. The depth obtained by the acoustic wave-equation-based earthquake location method is 6.35 km (Table 8), consistent with the result based upon the spectral-element moment tensor inversion. Fig. 9 shows the results of waveform fitting at two representative stations. We can observe that the synthetic waveforms generated at the final earthquake location have smaller phase shifts from the recorded data than the ones corresponding to the initial location do. This implies that we have obtained a more accurate location for the Big Bear earthquake. In addition,

Table 8. The iteratively updated hypocentre location of the 2004 Big Bear earthquake and the corresponding RMS value of the first *P*-wave traveltime residuals. The initial earthquake location is obtained from the SCSN catalogue.

Iteration	Longitude (°)	Latitude (°)	Depth (km)	RMS (s)
0	−116.8480	34.3097	1.230	0.33226
1	−116.8511	34.3109	5.547	0.13173
2	−116.8524	34.3110	5.753	0.13474
3	−116.8527	34.3111	5.938	0.13878
4	−116.8529	34.3112	6.077	0.14226
5	−116.8530	34.3112	6.175	0.14489
6	−116.8530	34.3113	6.241	0.14676
7	−116.8530	34.3113	6.283	0.14802
8	−116.8531	34.3113	6.310	0.14883
9	−116.8531	34.3113	6.327	0.14934
10	−116.8531	34.3113	6.338	0.14966
11	−116.8531	34.3113	6.344	0.14985
12	−116.8531	34.3113	6.348	0.14997
13	−116.8531	34.3113	6.350	0.15004
14	−116.8531	34.3113	6.351	0.15008

we can investigate the relationship between earthquake occurrence and seismic velocity providing that the earthquake is accurately located. Tong *et al.* (2014d) mapped the seismic velocity structures of the 1992 Landers earthquake area and the 2004 Big Bear earthquake is actually in the investigated region (Fig 8a). A vertical view of the *P*-wave velocity model recovered by Tong *et al.* (2014d) which passes through the 2004 Big Bear earthquake and the 1992 Landers earthquake is shown in Fig. 8(b). We can observe that the Big Bear earthquake is initially located in a high Vp anomaly close to the surface but its final location is in a transition zone between high Vp and low Vp structures. The inverted earthquake location with the acoustic wave-equation-based method is in agreement with the statement that many large or relatively large crustal earthquakes occurred in regions with significant seismic property variations (Tong *et al.* 2014d). The tomographic evidence also indicates the validity of the newly proposed earthquake location method.

5 DISCUSSION AND CONCLUSIONS

The full wavefield simulation honours the finite-frequency effects of the propagating seismic waves and accurately captures the interactions between seismic waves and complex (such as strongly heterogeneous) structures. These advantages prompted us to derive the acoustic wave-equation-based earthquake location method. Considering that the full 3-D seismic numerical modelling is always computationally demanding or even prohibitive, a 2.5-D version of this method is designed to lessen the computation burden. From the synthetic examples in Section 3, we
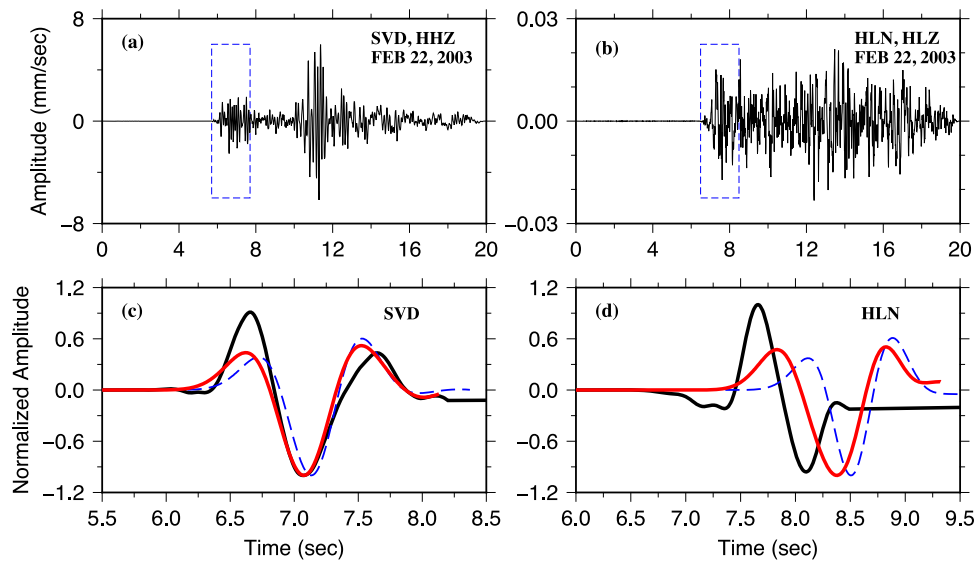

Figure 9. (a,b) Two vertical components of the raw data generated by the Big Bear earthquake and recorded at seismic stations SVD and HLN, respectively. The blue dashed boxes are the 2-s time windows for selecting the portions of the data for earthquake location. The time windows begin at the onset times of the first *P*-arrivals. (c) The black curve is the filtered data after applying a Butterworth filter between 0.1 and 1.3 Hz to the windowed seismogram in panel (a). The blue dashed and red curves are synthetic waveforms that are generated at the initial and final locations, respectively. The phase shifts of the synthetic waveforms from the observed data change from 0.17 to −0.07 s throughout the iterations. (d) The same as panel (c) but for seismic station HLN. Initially, the synthetic *P*-wave (blue dashed curve) is 0.65 s delayed from the observed data (black curve). After 14 iterations, the delay is reduced to 0.23 s.

generally learn three points. (1) The newly proposed method can precisely locate earthquake location if high-quality data and exact velocity model are ideally available. (2) High-frequency data has better resolving ability than low-frequency data. (3) If only an approximate velocity model is known, the acoustic wave-equation-based method probably finds a location which is not but around its actual location. Furthermore, the validity of the acoustic wave-equation-based earthquake location method in real applications is verified by applying it to relocate the 2004 Big Bear earthquake and comparing the result with the ones generated by other techniques such as the spectral-element moment tensor inversion of Liu *et al.* (2004).

The results of this study suggest that the 2.5-D version of the acoustic wave-equation-based earthquake location method can be independently used to locate earthquakes with computational efficiency and accuracy. However, it still needs more computational resources than Geiger's method does. As discussed in Section 2, the main advantage of the acoustic wave-equation-based technique is that it can accurately calculate the Fréchet derivatives, especially in complex velocity models. Since the earthquake location is iteratively updated, in future studies we can first use Geiger's method to get an initial location and then adopt the acoustic wave-equation-based method to refine the location. The combination of these two methods should reduce the computation cost. Furthermore, the velocity model is a key component in earthquake location. The extent to which we know the velocity model determines how accurately we can locate the earthquake. For a sole earthquake location inversion, the error in velocity model may trade-off with the inverted results. Therefore, a simultaneous inversion for velocity model and earthquake location may be necessary for obtaining a more accurate earthquake location. In addition, the 2.5-D approach suggests using 2-D forward modelling for 3-D hypocentre location. If the velocity model is very complex and the off-plane effects cannot be ignored, we can resort to the acoustic wave-equation-based earthquake location method based upon 3-D forward modelling. For the sake of conciseness, we put no emphasis on location uncertainty in this study. Readers can refer to Thurber (2014) for a thorough discussion on how to analyse the precision and accuracy of earthquake location.

In conclusion, the proposed acoustic wave-equation-based earthquake location method provides a new efficient way for accurately locating earthquakes especially when complex velocity models are present. We expect that it can be used in seismic tomography studies with passive data, earthquake source parameters (such as centroid-moment tensor) inversion (Kim *et al.* 2011), microseismic monitoring in the process of hydraulic fracturing, nuclear explosion monitoring, and many other fields. For the next stage, this acoustic wave-equation-based earthquake location technique can be further developed to take advantage of the full waveform content instead of using only the cross-correlation traveltime information as in this study.

REFERENCES

Alkhalifah, T., 2010. Acoustic wavefield evolution as a function of source location perturbation, *Geophys. J. Int.,* **183**(3), 1324–1331.

Bondar, I., Bergman, E., Engdahl, E.R., Kohl, B., Kung, Y.-L. & McLaughlin, K., 2008. A hybrid multiple event location technique to obtain ground truth event locations, *Geophys. J. Int.,* **175**(1), 185–201.

Castellanos, F. & van der Baan, M., 2013. Microseismic event locations using the double-difference algorithm, *CSEG Recorder,* **38**(3), 26–37.

Chen, H., Chiu, J.-M., Pujol, J., Kim, K., Chen, K.-C., Huang, B.-S., Yeh, Y.-H. & Chiu, S.-C., 2006. A simple algorithm for local earthquake location using 3D Vp and Vs models: test examples in the Central United States and in Central Eastern Taiwan, *Bull. seism. Soc. Am.,* **96**(1), 288–305.

Chen, P., Zhao, L. & Jordan, T.H., 2007. Full 3D tomography for the crustal structure of the Los Angeles region, *Bull. seism. Soc. Am.,* **97**(4), 1094–1120.

Dahlen, F.A., Nolet, G. & Hung, S.-H., 2000. Fréchet kernels for finite-frequency traveltimes—I. Theory, *Geophys. J. Int.,* **141**(1), 157–174.

Engdahl, E.R. & Lee, W.H.K., 1976. Relocation of local earthquakes by seismic ray tracing, *J. geophys. Res.,* **81**(23), 4400–4406.

Fichtner, A. & Trampert, J., 2011. Resolution analysis in full waveform inversion, *Geophys. J. Int.,* **187**(3), 1604–1624.

Font, Y., Kao, H., Lallemand, S., Liu, C.-S. & Chiao, L.-Y., 2004. Hypeocentre determination offshore of eastern Taiwan using the Maximum Intersection method, *Geophys. J. Int.,* **158**(2), 655–675.

Ge, M., 2003a. Analysis of source location algorithms Part I: Overview and non-iterative methods, *J. Acoust. Emiss.,* **21,** 14–28.

Ge, M., 2003b. Analysis of source location algorithms Part II: Iterative methods, *J. Acoust. Emiss.,* **21,** 29–51.

Geiger, L., 1910. Herdbestimmung bei Erdbeben aus den Ankunftszeiten, *Nachrichten von der Gesellschaft der Wissenschaften zu Gottingen, Mathematisch-Physikalische Klasse,* **1910,** 331–349.

Geiger, L., 1912. Probability method for the determination of earthquake epicenters from the arrival time only, *Bull. St. Louis Univ.,* **8,** 60.

Horiuchi, S., Negishi, H., Abe, K., Kamimura, A. & Fujinawa, Y., 2005. An automatic processing system for broadcasting earthquake alarms, *Bull. seism. Soc. Am.,* **95**(2), 708–718.

Huang, Z. & Zhao, D., 2013. Relocating the 2011 Tohoku-oki earthquakes (M 6.0–9.0), *Tectonophysics,* **586,** 35–45.

Kim, Y., Liu, Q. & Tromp, J., 2011. Adjoint centroid-moment tensor inversions, *Geophys. J. Int.,* **186**(1), 264–278.

Komatitsch, D. & Tromp, J., 1999. Introduction to the spectral element method for three-dimensional seismic wave propagation, *Geophys. J. Int.,* **139**(3), 806–822.

Komatitsch, D., Liu, Q., Tromp, J., Suss, P., Stidham, C. & Shaw, J.H., 2004. Simulations of ground motion in the Los Angeles Basin based upon the spectral-element method, *Bull. seism. Soc. Am.,* **94**(1), 187–206.

Lin, G., 2013. Three-dimensional seismic velocity structure and precise earthquake relocations in the Salton Trough, southern California, *Bull. seism. Soc. Am.,* **103**(5), 2694–2708.

Liu, Q. & Gu, Y.J., 2012. Seismic imaging: from classical to adjoint tomography, *Tectonophysics,* **566–567,** 31–66.

Liu, Q., Polet, J., Komatitsch, D. & Tromp, J., 2004. Spectral-element moment tensor inversions for earthquakes in southern California, *Bull. seism. Soc. Am.,* **94**(5), 1748–1761.

Marquering, H., Dahlen, F. & Nolet, G., 1999. Three-dimensional sensitivity kernels for finite-frequency traveltimes: the banana-doughnut paradox, *Geophys. J. Int.,* **137**(3), 805–815.

Maxwell, S.C., Rutledge, J., Jones, R. & Fehler, M., 2010. Petroleum reservoir characterization using downhole microseismic monitoring, *Geophysics,* **75**(5), 75 A129–75 A137.

Miksat, J., Muller, T.M. & Wenzel, F., 2008. Simulating three-dimensional seismograms in 2.5-dimensional structures by combining two-dimensional finite difference modelling and ray tracing, *Geophys. J. Int.,* **174**(1), 309–315.

Milne, J., 1886. *Earthquakes and Other Earth Movements,* Appleton.

Pesicek, J.D., Child, D., Artman, B. & Cieslik, K., 2014. Picking versus stacking in a modern microearthquake location: comparison of results from a surface passive seismic monitoring array in Oklahoma, *Geophysics,* **79**(6), KS61–KS68.

Poliannikov, O.V., Prange, M., Malcolm, A.E. & Djikpesse, H., 2014. Joint location of microseismic events in the presence of velocity uncertainty, *Geophysics,* **79**(6), KS51–KS60.

Prugger, A.F. & Gendzwill, D.J., 1988. Microearthquake location: a nonlinear approach that makes use of a simplex stepping procedure, *Bull. seism. Soc. Am.,* **78**(2), 799–815.

Rabinowitz, N., 1988. Microearthquake location by means of nonlinear simplex procedure, *Bull. seism. Soc. Am.,* **78**(1), 380–384.

Rawlinson, N., Pozgay, S. & Fishwick, S., 2010. Seismic tomography: a window into deep Earth, *Phys. Earth planet. Inter.,* **178**(3–4), 101–135.

Rickers, F., Fichtner, A. & Trampert, J., 2013. The Iceland-Jan Mayen plume system and its impact on mantle dynamics in the North Atlantic region: evidence from full-waveform inversion, *Earth planet. Sci. Lett.,* **367**, 39–51.

Schaff, D.P., Bokelmann, G.H.R., Ellsworth, W.L., Zanzerkia, E., Waldhauser, F. & Beroza, G.C., 2004. Optimizing correlation techniques for improved earthquake location, *Bull. seism. Soc. Am.,* **94**(2), 705–721.

Sumiejski, L., Thurber, C. & DeShon, H.R., 2009. Location of eruption-related earthquake clusters at Augustine Volcano, Alaska, using station-pair differential times, *Geophys. J. Int.,* **176**(3), 1017–1022.

Tape, C., Liu, Q. & Tromp, J., 2007. Finite-frequency tomography using adjoint methods-Methodology and examples using membrane surface waves, *Geophys. J. Int.,* **168**(3), 1105–1129.

Tape, C., Liu, Q., Maggi, A. & Tromp, J., 2009. Adjoint tomography of the southern California crust, *Science,* **325,** 988–992.

Tape, C., Liu, Q., Maggi, A. & Tromp, J., 2010. Seismic tomography of the southern California crust based on spectral-element and adjoint methods, *Geophys. J. Int.,* **180**(1), 433–462.

Thurber, C.H., 1985. Nonlinear earthquake location: theory and examples, *Bull. seism. Soc. Am.,* **75**(3), 779–790.

Thurber, C.H., 2014. Earthquake, location techniques, in *Encyclopedia of Earth Sciences Series,* pp. 201–207, ed. Gupta, H.K., Springer.

Tong, P., Zhao, D. & Yang, D., 2011. Tomography of the 1995 kobe earthquake area: comparison of finite-frequency and ray approaches, *Geophys. J. Int.,* **187**(1), 278–302.

Tong, P., Chen, C.-W., Komatitsch, D., Basini, P. & Liu, Q., 2014a. High-resolution seismic array imaging based on an SEM-FK hybrid method, *Geophys. J. Int.,* **197**(1), 369–395.

Tong, P., Komatitsch, D., Tseng, T.-L., Hung, S.-H., Chen, C.-W., Basini, P. & Liu, Q., 2014b. A 3-D spectral-element and frequency-wave number (SEM-FK) hybrid method for high-resolution seismic array imaging, *Geophys. Res. Lett.,* **41**(20), 7025–7034.

Tong, P., Zhao, D., Yang, D., Yang, X., Chen, J. & Liu, Q., 2014c. Wave-equation-based travel-time seismic tomography—Part 1: method, *Solid Earth,* **5,** 1151–1168.

Tong, P., Zhao, D., Yang, D., Yang, X., Chen, J. & Liu, Q., 2014d. Wave-equation-based travel-time seismic tomography—Part 2: Application to the 1992 Landers earthquake area, *Solid Earth,* **5,** 1169–1188.

Tromp, J., Tape, C. & Liu, Q., 2005. Seismic tomography, adjoint methods, time reversal and banana-doughnut kernels, *Geophys. J. Int.,* **160**(1), 195–216.

Waldhauser, F. & Ellsworth, W.L., 2000. A double-difference earthquake location algorithm: method and application to the Northern Hayward Fault, California, *Bull. seism. Soc. Am.,* **90**(6), 1353–1368.

Wen, L. & Long, H., 2010. High-precision location of North Korea's 2009 nuclear test, *Seism. Res. Lett.,* **81**(1), 26–29.

Wessel, P. & Smith, W. H.F., 1991. Free software helps map and display data, *EOS, Trans. Am. geophys. Un.,* **72**(41), 441–446.

Zhang, H., Thurber, C. & Rowe, C., 2003. Automatic P-wave arrival detection and picking with multiscale wavelet analysis for single-component recordings, *Bull. seism. Soc. Am.,* **93**(5), 1904–1912.

Zhang, M. & Wen, L., 2015. Seismological evidence for a low-yield nuclear test on 12 May 2010 in North Korea, *Seism. Res. Lett.,* **86**(1), 138–145.

Zhu, H., Bozdag, E., Peter, D. & Tromp, J., 2012. Structure of the European upper mantle revealed by adjoint tomography, *Nat. Geosci.,* **5,** 493–498.